



Effect of Cr content on the corrosion resistance of Ni–Cr–P coatings for PEMFC metallic bipolar plates

Uttam K. Chanda¹ · Satya Prakash Padhee¹ · Anil D. Pathak¹ · Sudesna Roy² · Soobhankar Pati¹

Received: 22 July 2019 / Accepted: 19 September 2019 / Published online: 27 September 2019
© The Author(s) 2019

Abstract

In here, we report on the pulse electrodeposition of nickel–chromium–phosphorous (Ni–Cr–P) coatings on AISI 1020 low carbon steel using an aqueous electrolyte consisting of NiCl₂, CrCl₃, and NaH₂PO₂. We evaluated the effectiveness of Ni–Cr–P coatings for polymer electrolyte membrane fuel cell metallic bipolar plates. Coatings deposited at pH 3.0 and room temperature show nearly three orders improvement in corrosion resistance compared to bare AISI 1020. The corrosion current (I_{corr}) of Ni–Cr–P samples coated at 25 °C is 1.16×10^{-4} A/cm², while that of bare carbon steel is 1.05×10^{-2} A/cm². The improvement in corrosion resistance is due to the increase in Cr content in the Ni–Cr–P coatings. Cr forms a stable oxide barrier layer and inhibits pitting corrosion. The interfacial contact resistance increases with an increase in Cr content and immersion time in the corrosion media. The increase in interfacial contact resistance is also due to the formation of a stable oxide barrier.

Keywords PEM fuel cells · Bipolar plates · Pulse electrodeposition · Cyclic voltammetry · Potentiodynamic polarization · Interfacial contact resistance · AISI 1020 low-carbon steel

Introduction

Bipolar plate (BPP) plays a key role in a “polymer electrolyte membrane (PEM) fuel cell stack.” It prevents the interaction of the anodic and cathodic gases, distributes the anodic and cathodic gases uniformly, and electrically connects the adjacent cells. Material selection for the BPPs is crucial because the reactant and exhaust gases are humid and corrode the bipolar plates. Corroded BPPs exhibit high interfacial contact resistance between the gas diffusion layer (GDL) and the bipolar plate [1]. Therefore, for most commercial application, graphite is being used to date despite its high material and manufacturing cost. However, for large-scale adoption

of PEM fuel cell in automobiles, it is essential to replace the graphite bipolar plates with cost-effective and durable materials. The US Department of Energy (USDoE) target for the year 2020 is \$3.0/kW for automotive applications. The low target set by USDoE limits the use of exotic materials for BPPs [2]. Hence, low-cost metallic bipolar plates are more likely to replace graphitic plates.

Metals such as titanium [3], copper [4], aluminum [5], stainless steel [6], carbon steel [7–12], and various other alloys [13, 14] have been evaluated for PEM fuel cell BPPs. Most of these studies conclude that although the cost of manufacturing is low for metallic bipolar plates, the corrosion resistance is also low and hence are not suitable for BPPs. The metallic bipolar plates corrode due to interaction with humid gases. During PEM fuel cell operation at 80 °C, the metal (M⁺) ions tend to leach out from the surface of metallic BPPs. The sulfonate sites present in the polymer electrolyte membrane have a high affinity toward M⁺ ions than that toward H⁺ ions [15], and this is detrimental to protonic conductivity of the polymer electrolyte membrane. Further, when operated for longer duration SO₄²⁻ and F⁻ ions leach-out from the electrolyte {perfluorosulfonic acid (C₉HF₁₇O₅S)} and make an aggressive environment near the BPP accelerating the corrosion rate.

Electronic supplementary material The online version of this article (<https://doi.org/10.1007/s40243-019-0158-8>) contains supplementary material, which is available to authorized users.

✉ Soobhankar Pati
spati@iitbbs.ac.in

¹ School of Minerals, Metallurgical and Materials Engineering, Indian Institute of Technology, Bhubaneswar 752050, India

² School of Mechanical Engineering, Kalinga Institute of Industrial Technology, Bhubaneswar 751024, India

Surface modification of the metallic BPPs increases the corrosion resistance and durability [16]. Although durability increases, it adds to the manufacturing cost. That said it is imminent that surface modification of metallic bipolar plates is necessary before they can be used in a PEM fuel cell stack.

Among all the proposed metals for BPPs, steel is the most promising candidates for surface-modified metallic BPP as it is inexpensive and widely available. Steel BPPs are fabricated by stamping the cathode gas and anode gas flow field on two ~0.2 mm thick sheets, followed by joining them via laser or spot welding [17, 18]. This method of making BPPs reduces not only the stack's cost of manufacturing but also the volume significantly. The surface modification techniques required for improving the corrosion resistance of these steel bipolar plates are a pack-chromizing [7–9, 12], and closed field unbalanced magnetron sputter ion plating (CFUMSIP) [10] with Ni coating based pretreatment and electroplating.

In our previous work [19], we proposed a cost-effective and non-capital-intensive electroplating process to keep the cost of BPPs affordable. We reported on the microstructural, electrical, and corrosion properties of electrodeposited Ni–Cr–P coatings on AISI 1020 low-carbon steel. Electrodeposited chromium-based alloys show good corrosion resistance along with low interfacial contact resistance (ICR) suitable for PEM fuel cell application. Cr on the surface oxidizes to form a barrier layer composed of Cr_2O_3 and CrO_3 , and these oxides improve corrosion resistance. Further addition of phosphorus into the coating improves the corrosion resistance of the coating. However, in a humid environment, Cr_2O_3 and CrO_3 inhomogeneously convert into $\text{Cr}(\text{OH})_3$ or other hydrated oxides. The F^- ions from the electrolyte membrane attack the hydroxides (or hydrated oxides) in the barrier layer to form pits at the surface [20]. Therefore, tuning the composition and microstructure is crucial in improving the durability of the BPPs.

In this work, we report on the tuning of composition and microstructure via electrodeposition and its effect on the corrosion resistance and interfacial contact resistance. The amount of Cr in the coating is critical for deciding not only corrosion but also the interfacial contact resistance. With an increase in Cr content, the corrosion decreases but the interfacial contact resistance (ICR) between the gas diffusion layer (GDL) and the BPP increases.

Experimental

Substrate preparation

We procured and used a commercial-grade Fe-based AISI 1020 low-carbon steel plate with a chemical composition (in wt %) of C-0.2, P-0.04, Mn-0.6, S-0.05 and balance Fe as the

BPP substrate. We prepared the surface for electrodeposition by cutting AISI 1020 low-carbon steel plate into small coupons of dimension 45 mm × 15 mm × 1 mm and polishing the coupons with SiC papers followed by 1 μm alumina suspension. Before the pretreatment process, we ultrasonicated the substrate using ethanol and washed it with distilled water.

Pretreatment and electroplating

We performed anodic cleaning and surface activation for better cohesion between the substrate and the coating. During the anodic cleaning process, we passed a constant anodic current of 0.05 A/cm² through the substrate in an alkaline solution [21, 22]. Subsequently, we dipped the substrate for 15 s in a dilute acidic solution containing HCl and H_2SO_4 in a ratio of 3:1 (by wt%). Before Ni–Cr–P electroplating, we deposited an intermediate layer of nickel on the substrate using an aqueous solution containing $\text{NiSO}_4 \cdot 6\text{H}_2\text{O}$ (0.8 M), $\text{NiCl}_2 \cdot 6\text{H}_2\text{O}$ (0.5 M) and H_3BO_3 (0.5 M) [23].

We prepared the electrolyte solution using a mixture of aprotic solvent (*N,N*-dimethylformamide) and water (1:1 v/v). We used salts and additives, as mentioned in our previous work [19], to prepare a fresh electrolyte solution for each deposition cycle. We placed the beaker containing the electrolyte solution in an ice bath and stirred it at 200 rpm during the electroplating. We carried out the electroplating using Agilent N6700B DC low modular power source applying a pulse current density (I_{ON}) of 0.1 A/cm² with repeated T_{ON} and T_{OFF} for about 5 and 1 ms, respectively. We measured the temperature using a digital thermometer during the electroplating process.

Microstructural, compositional, phase and electrochemical characterization

We analyzed the microstructure and elemental composition using Carl-Zeiss Merlin II FESEM and EDS from Oxford Instruments, respectively. We studied phase analysis using PANalytical Empyrean X-ray diffractometer (XRD). To suppress the interference from the carbon steel substrate, we scanned the coating samples at a grazing incidence angle of 1.5° over a 2θ range of 20°–95°.

We used Metrohm Autolab PGSTAT302N for cyclic voltammetry and potentiodynamic polarization. We conducted cyclic voltammetry (CV) by sweeping between ± 1 V at a scan rate of 10 mV/s, of four different aqueous electrolytic solutions (10 mM $\text{NiCl}_2 \cdot 6\text{H}_2\text{O}$, 10 mM $\text{CrCl}_3 \cdot 6\text{H}_2\text{O}$, an equimolar mixture of both the solution and a combinational mixture solution of 10 mM $\text{NiCl}_2 \cdot 6\text{H}_2\text{O}$, 10 mM $\text{CrCl}_3 \cdot 6\text{H}_2\text{O}$, and 10 mM $\text{NaH}_2\text{PO}_4 \cdot \text{H}_2\text{O}$). We used a platinum disk, platinum wire, and Ag/AgCl electrode as the working, auxiliary, and reference electrode, respectively.

For potentiodynamic analysis, we chose an AISI 1020 substrate with an area of 2.25 cm^2 as a working electrode. We used platinum wire and Ag/AgCl as an auxiliary and a reference electrode, respectively. To simulate the PEM fuel cell environment, we used an electrolyte for corrosion testing comprising of $0.5 \text{ M H}_2\text{SO}_4$ and 2.0 ppm HF at 80°C . We conducted potentiodynamic scans (scan rate: 0.1 mV/s) by purging H_2 and air into the electrolyte to simulate the anodic and cathodic environment, respectively.

Interfacial contact resistance

Interfacial contact resistance (ICR) is the area-specific resistance between the BPPs and gas diffusion layer (GDL) in the PEM fuel cell. Researchers have standardized the method of measuring ICR between the BPPs and gas diffusion layer (GDL) in the PEM fuel cell [24], and here we used

a similar technique, reported in previous studies [19]. In this work, we prepared the surface of bare AISI low-carbon steel, and Ni–Cr–P coated AISI low-carbon steel with GDL after immersing them in an $0.5 \text{ M H}_2\text{SO}_4$ and 2 ppm HF at 80°C for a certain duration. We measured the contact resistance of the two layers by applying a compaction pressure of 150 N/cm^2 during the measurement.

Results and discussion

Cyclic voltammetry analysis

Figure 1 shows the current density vs. voltage plot for the four electrolytes and inset in each figure shows the area under the curve for the four electrolytes during the oxidation cycle. The cyclic voltammogram of electrolyte solution containing

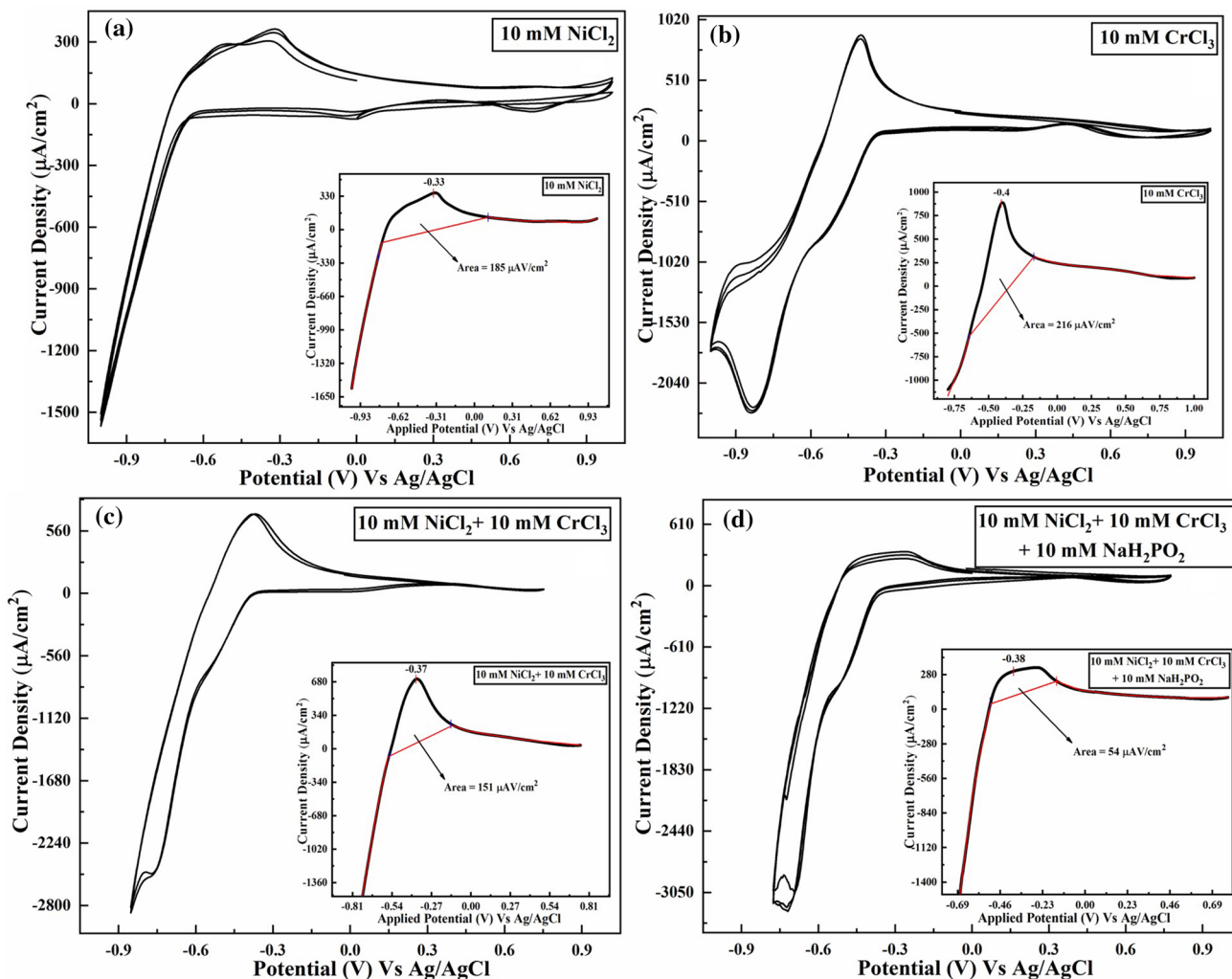
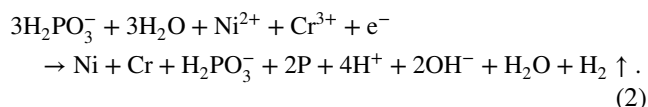
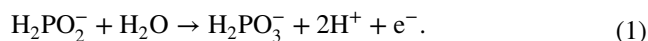


Fig. 1 Cyclic voltammograms of **a** 10 mM CrCl_3 , **b** 10 mM NiCl_2 , **c** 10 mM CrCl_3 and 10 mM NiCl_2 , and **d** combination of 10 mM CrCl_3 , 10 mM NiCl_2 and NaH_2PO_2 aqueous solution at scan-rate of 10 mV/s

10 mM NiCl₂ (Fig. 1a) shows a prominent reduction peak at -550 mV indicating the reduction of Ni²⁺ to Ni⁰ at the cathode. In the case of 10 mM CrCl₃ (Fig. 1b), there is a sudden increase in current density during the reverse scan at around -300 mV. The sudden increase in current density is most likely due to the reduction of [Cr(H₂O)₆]³⁺ to [Cr(H₂O)₆]²⁺, while change in slope at around -600 mV is due to the formation of [Cr(H₂O)₆]²⁺ from [Cr(H₂O)₆]³⁺, and finally formation of [Cr(H₂O)₆]⁰ at a potential of -800 mV, which is close to hydrogen evolution potential [25]. Figure 1c shows the cyclic voltammogram of an equimolar mixture 10 mM CrCl₃ and 10 mM NiCl₂. It is similar to the cyclic voltammogram of the electrolyte solution containing 10 mM NiCl₂. In an aqueous solution of CrCl₃, Cr³⁺ ion exists in the form of solvated ion complex, [Cr(H₂O)₆]³⁺, and hence the reduction of [Cr(H₂O)₆]³⁺ complex is difficult [25].

Figure 1d shows the change in oxidation and reduction peak current density with the addition of equimolar NaH₂PO₂ into a solution of 10 mM CrCl₃ and 10 mM NiCl₂. The oxidation peak-current density, during the reverse sweep, decreases with the addition of phosphorus. Although we emphasize the details on corrosion analysis in a simulated fuel cell environment later, the reduction in current density in cyclic voltammogram shows that the addition of phosphorus increases the corrosion resistance of the coating.

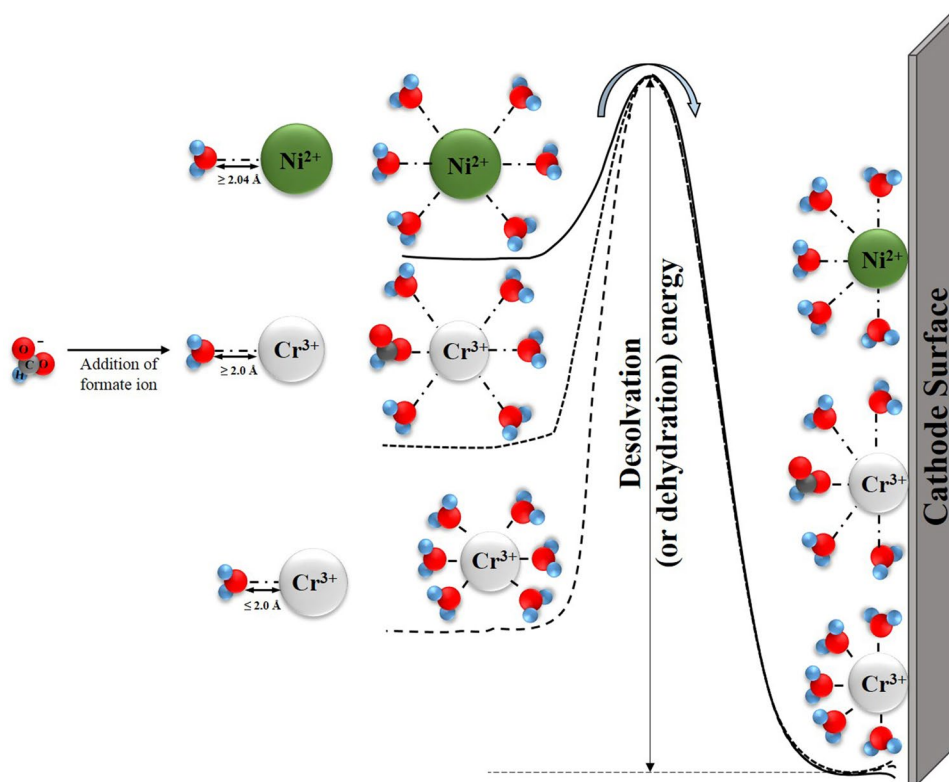
The overall reactions involved in the electro-reduction process can be expressed as [26] follows:



The phosphorus generated in the above reaction reacts with Ni-Cr in the deposit to form a Ni-Cr-P coating on the substrate.

Electroreduction in an aqueous electrolyte is a nucleophilic substitution reaction where electron from the cathodic surface replaces H₂O molecule from the complex. Figure 2 shows the schematic representation of the electroreduction process of nickel and chromium formation with the solvated metal ion in aqueous solution and desolvation (or dehydration) energy required for [Ni(H₂O)₆]²⁺ and [Cr(H₂O)₆]³⁺ solvated ions. The solvated complex is a compact regular octahedron structure and plays a major role in the electroreduction process [27, 28]. The distance between the Cr³⁺ ion and the water molecule is ≤ 2.0 Å, while that between Ni²⁺ ion and H₂O is ≥ 2.04 Å [27]. Nickel solvated ions [Ni(H₂O)₆]²⁺ require lesser dehydration energy as compared to the [Cr(H₂O)₆]³⁺ solvated ion because of the larger Ni²⁺-H₂O bond length compared to Cr³⁺-H₂O bond length. That said, the adding of complexing ligands (such as HCOO⁻, C₂O₄²⁻ or C₂H₃O₂⁻) to the electrolyte increases the Cr³⁺-H₂O bond length in the solvated ion, thereby increasing the rate of Cr³⁺ electroreduction.

Fig. 2 Schematic representation of desolvation (or dehydration) energy of [Ni(H₂O)₆]²⁺ solvated ion denoted by solid line; of [Cr(H₂O)₅HCOO]²⁺ solvated ion denoted by dotted line; and of [Cr(H₂O)₆]³⁺ solvated ion denoted by dashed line



In a cyclic voltammogram, the area under the curve during the oxidation cycle is directly proportional to the diffusion of reduced species into the bulk of the electrolyte solution and vice versa. Comparing the insets in Fig. 1, we observe that the area under the curve with CrCl_3 is higher than NiCl_2 . It indicates that Cr-containing complexes oxidize easily compared to Ni-containing complexes. On the other hand, the area under the curve for $\text{CrCl}_3\text{-NiCl}_2\text{-NaH}_2\text{PO}_2$ electrolyte is lower compared to only CrCl_3 or NiCl_2 . The resistance to oxidation, particularly in the case of $\text{CrCl}_3\text{-NiCl}_2\text{-NaH}_2\text{PO}_2$ electrolyte, suggests that reduced species of this electrolyte are more stable and may offer better resistance to corrosion compared to pure Ni or Cr in a harsher environment.

Electrodeposition

Figure 3 shows the micrograph of Ni–Cr–P coating deposited from electrolytic baths at various pH. Figure 3a–c shows the surface microstructure of the coating electrodeposited at pH 2.0 (± 0.15), pH 2.5 (± 0.15), and pH 3.0 (± 0.15),

respectively. It is evident that the coatings deposited at pH 2.0 (± 0.15) and pH 2.5 (± 0.15) are non-uniform with surface cracks. However, when pH is increased to 3.0 (± 0.15), the coatings are uniform and dense. The non-uniform deposit at pH 2.0 (± 0.15) and pH 2.5 coating (± 0.15) is most likely due to the high concentration of H^+ ions near the cathode surface at lower pH [29]. We infer that increasing the pH lowers the H_2 gas evolution during electrodeposition.

During the electrodeposition process, if we apply a potential across the electrodes, solvated metal ions migrate towards the cathode surface where they take up the electrons and reduce to deposit as metal. However, due to the undesirable reaction, at the cathode surface, the pH of the electrolyte increases within the electrical double layer. The evolution of H_2 gas at the cathode surface creates cracks and voids in the coating. With further increase in pH, the hydroxyl ions near the cathode surface result in the formation of $\text{Cr}(\text{OH})_3$ and some amount of $\text{Ni}(\text{OH})_2$. The coating surface becomes dark in appearance and decrease in reduction rate as insoluble $\text{Cr}(\text{OH})_3$ blocks the cathode surface [30]. The rest of the insoluble hydroxides precipitate

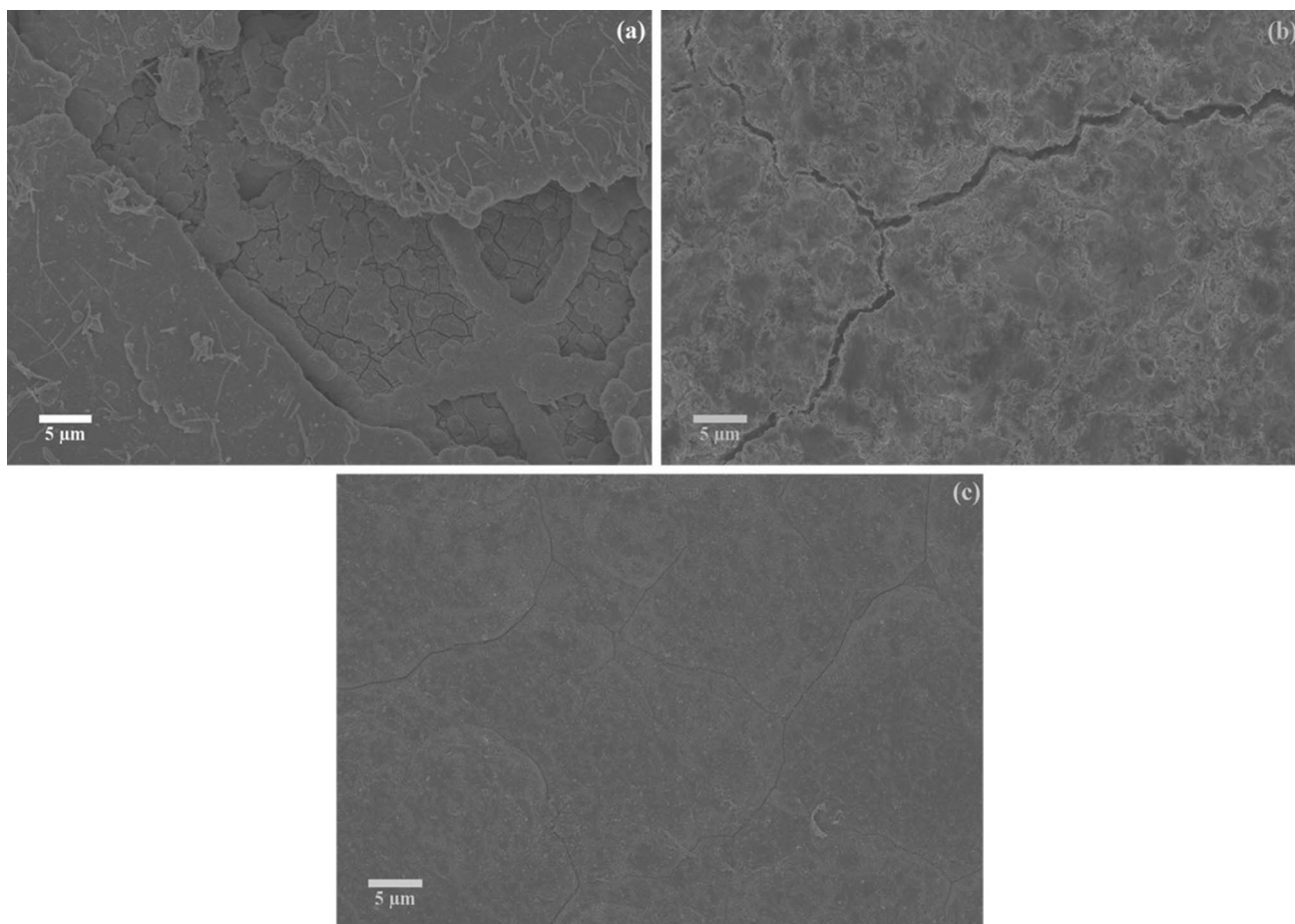


Fig. 3 FESEM image of pulse-electrodeposited Ni–Cr–P alloy at **a** pH 2.0 (± 0.15), **b** pH 2.5 (± 0.15), and **c** pH 3.0 (± 0.15); having constant temperature (25 °C)

making the electrolyte solution sludgy. Therefore, even in the presence of an aprotic solvent, the accumulation of H^+ ions is inevitable at low pH. The evolution of H_2 decreases by increasing the pH, increasing beyond pH 3.0 (± 0.15), but it leads to precipitation of insoluble hydroxides.

Figures 4 and 5 show the microstructure and composition of the coatings, respectively, electrodeposited at a pH of 3.0 at various temperatures. Although the microstructure is similar, there is a change in the composition of the coatings. The Cr concentration in the coating increases with increase in electrodeposition temperature. The increase in Cr content with temperature is elucidated by combining the Butler–Volmer equation along with Faraday’s law of electrolysis [22]. For binary alloy system, per unit time the amount of metal deposited, W , is given by

$$\frac{W_1}{W_2} = \frac{i_{0,1}M_1n_2}{i_{0,2}M_2n_1} \exp \left[-\frac{F}{2RT}(n_1j_1 - n_2j_2) \right], \quad (3)$$

where M is the atomic weight of the metal, n is the number of moles, F is the Faraday constant, i_0 is the exchange

current density, R is the gas constant, j is the overpotential, and T is the absolute temperature.

The rate constant for charge transfer during reduction Cr and Ni complexes is considered to be in the same order. Therefore, it is evident from Eq. (3) that the amount of Cr deposited increases with increase in temperature. Although the coating with high Cr content has a superior corrosion-resistant oxide scale, the internal stress in the coating increases with an increase in Cr content. The increase in the internal stress increases the number of micro-cracks on the coating surface [30, 31]. Therefore, too much or too little Cr in the coating is harmful to the life of the bipolar plates.

Phase analysis

Figure 6 shows the X-ray diffraction (XRD) spectra of AISI 1020 carbon steel substrate and the grazing incidence (GI) XRD of Ni–Cr–P alloys coated at different temperatures. The bare AISI 1020 substrate shows peaks at different 2θ , corresponding to the reference pattern [JCPDS 06-0696]. The GI-XRD spectra of different Ni–Cr–P coating samples show diffuse spectra at 2θ of 44.53° . The diffuse spectra

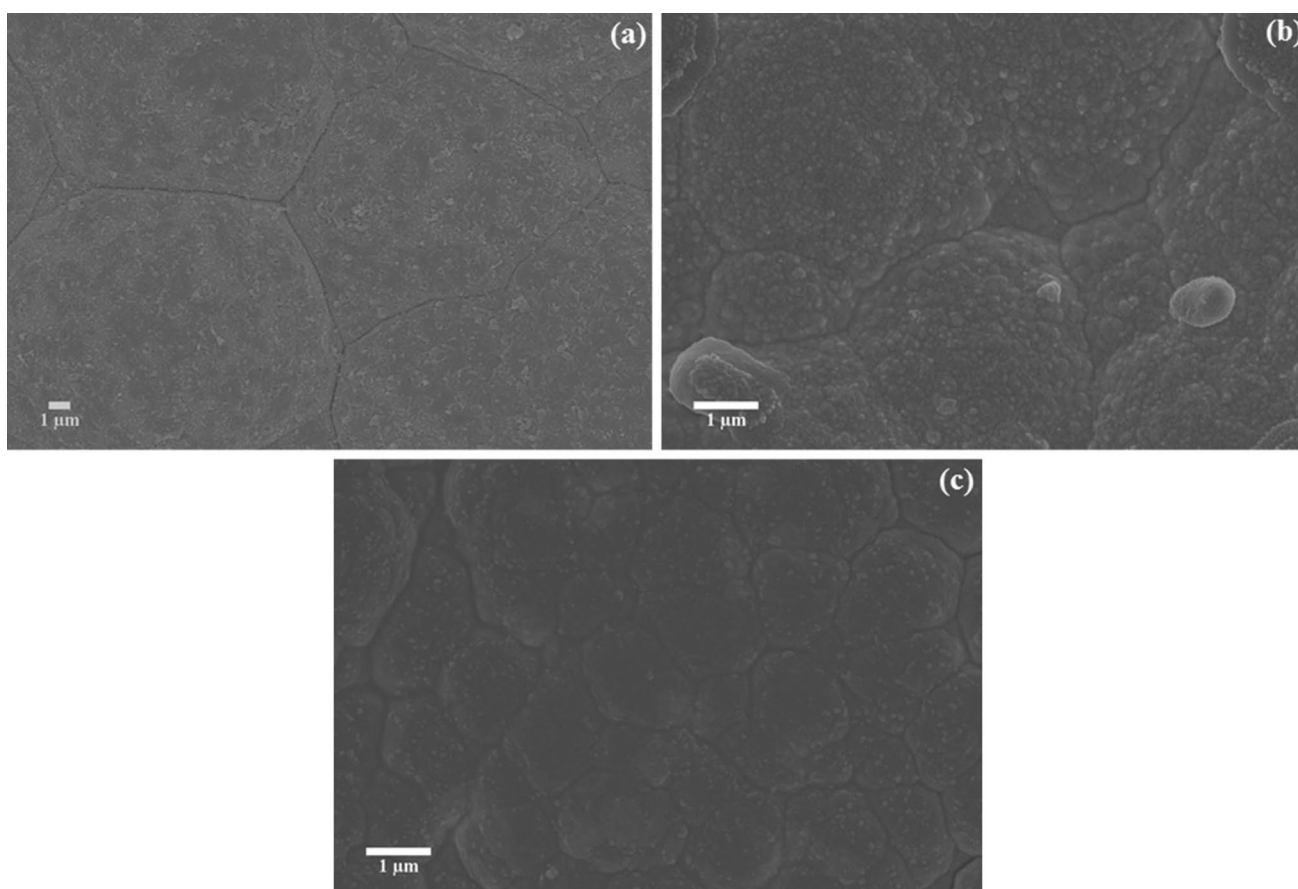
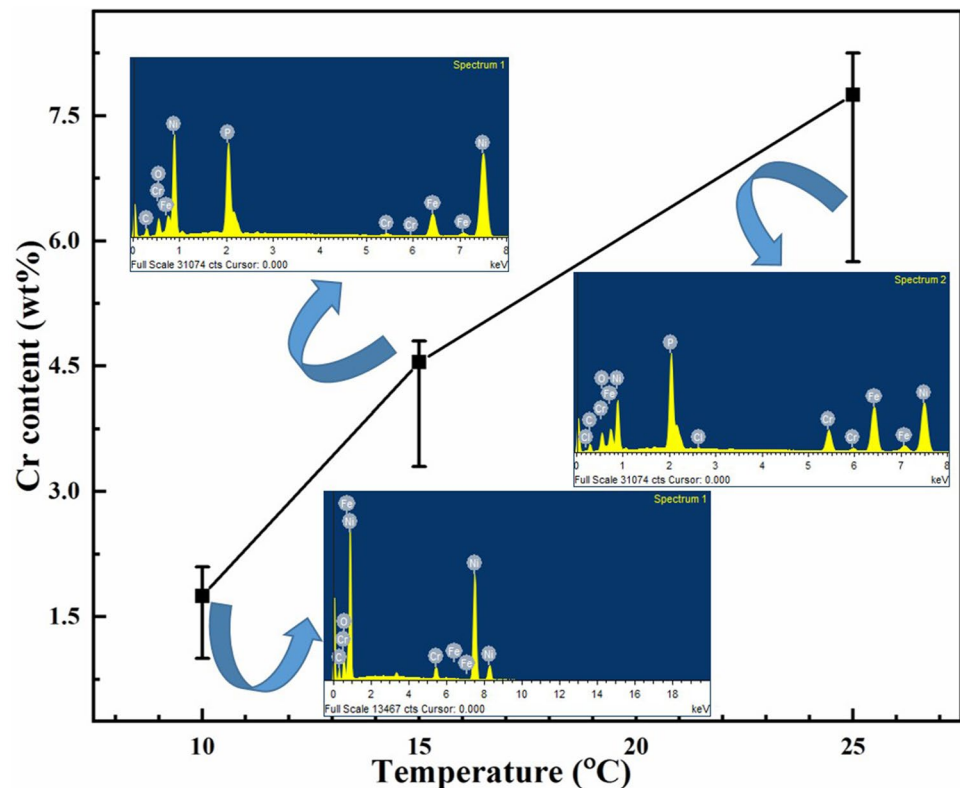


Fig. 4 FESEM image of pulse-electrodeposited Ni–Cr–P alloy at **a** 10 °C (± 3 °C), **b** 15 °C (± 3 °C), and **c** 25 °C (± 3 °C); having constant pH (3.0)

Fig. 5 Variation of chromium content with temperature during Ni–Cr–P electrodeposition



indicate the amorphous nature of different coating samples. The amorphous spectra are due to the presence of elemental phosphorus, which increases the crystalline defect in the coatings [19].

Corrosion analysis

Figure 7 shows the polarization curves of bare AISI 1020 low-carbon steel and Ni–Cr–P coatings electrodeposited at various temperatures, in the anodic and cathodic operating environment. In the anodic and cathodic environment, AISI 1020 carbon steel shows active behavior while Ni–Cr–P coatings show a relatively passive behavior. During potentiodynamic polarization measurements in simulated anodic and cathodic PEM fuel cell environment, the current density with the voltage of AISI 1020 increases rapidly, while Ni–Cr–P coated samples show constant current density after an initial increase. This indicates that the bare AISI 1020 shows an active behavior, while the Ni–Cr–P coated sample shows a passive behavior. Bare AISI 1020 low-carbon steel will dissolve in the electrolyte as it does not form any stable oxide layer. On the other hand, Ni–Cr–P coated plates are expected to form a protective oxide layer during the initiation of corrosion and this oxide layer will protect the substrate from corroding further.

Table 1 shows the polarization parameters of the bare substrates and coatings in both anodic and cathodic

environments. Bare AISI 1020 is not corrosion resistant in simulated PEM fuel cell environment. The corrosion rate of AISI 1020 decreased with electrodeposition of Ni–Cr–P coatings on the surface. The reason for the increase in corrosion resistance is due to the formation of a protective oxide layer of Cr and precipitation of Cr_3P phase at the grain boundaries, which suppresses pitting corrosion. Although the corrosion resistance increases, the chromium present in the coating at times forms an incoherent cracked passive layer with a large number of cation vacancies. The fluoride ions present in the electrolyte migrate through the cation vacancies. Moreover, unwanted pinholes and micro-cracks in the coating surface act as the active sites for pitting corrosion. We have elucidated the corrosion pathway Ni–Cr–P coatings in PEM fuel cell environment in our previous study [19].

The corrosion rate of Ni–Cr–P coatings in anodic and cathodic environment decreased with increasing the electrodeposition temperature. Increasing the temperature increases the Cr content, and hence the amount of Cr_3P phase also increases in the coatings. It is well known that Cr_3P decreases the sites for pitting corrosion [19].

The corrosion rate obtained in this study for bare and coated AISI 1020 is somewhat higher compared to previous reports [7–12]. For instance, Bai et al. [7, 12] showed that the corrosion current of bare steel sample is 6.34×10^{-4} A/cm² while Ni-electroplated pack chromized carbon steel

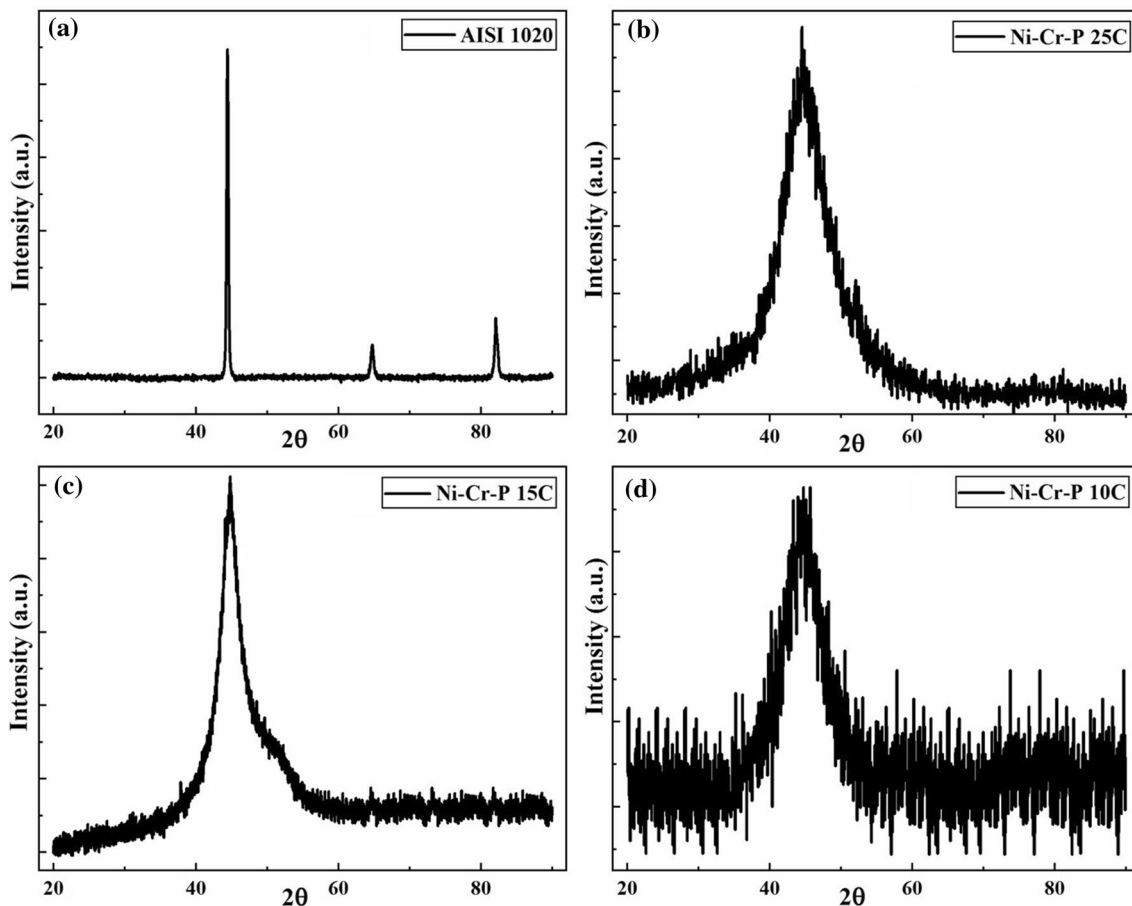


Fig. 6 XRD spectra of **a** AISI 1020 low-carbon steel, and Ni-Cr-P alloy pulse-electrodeposited at **b** 25 °C (± 3 °C), **c** 15 °C (± 3 °C), and **d** 10 °C (± 3 °C), having constant pH (3.0)

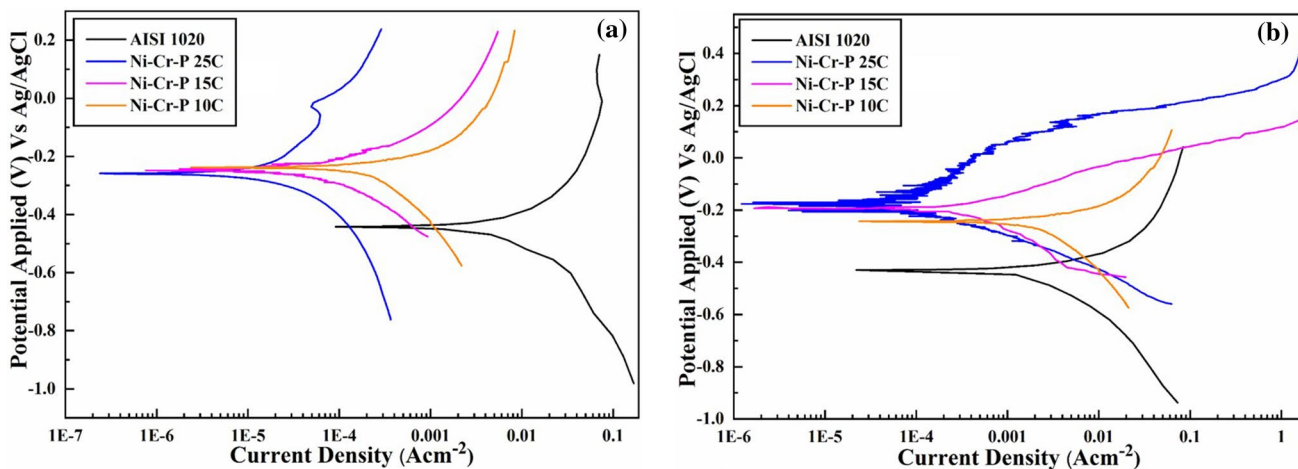


Fig. 7 Potentiodynamic polarization behavior of AISI 1020 low-carbon steel and Ni-Cr-P coated samples, electrodeposited at various temperatures, in 0.5 M H₂SO₄ and 2 ppm HF at 80 °C and scan-rate 0.1 mV/s, **a** anodic (H₂ purging) environment, **b** cathodic (air purging) environment

Table 1 Summary of chromium content, corrosion parameters, and ICR of AISI 1020 and Ni–Cr–P specimens, electrodeposited at various temperatures

Samples	Cr (wt%)	Anodic environment (H ₂ purging)			Cathodic environment (air purging)			Interfacial contact resistance (mΩ)				
		OCP (V)	E _{corr} (V)	I _{corr} (A/cm ²)	OCP (V)	E _{corr} (V)	I _{corr} (A/cm ²)	Immersion time (h)				
								00	01	02	03	04
AISI 1020	–	–0.44	–0.44	1.05 × 10 ^{–2}	–0.44	–0.42	3.7 × 10 ^{–2}	53.24	49.53	–	–	–
Ni–Cr–P 25C	7.75	–0.26	–0.25	1.16 × 10 ^{–4}	–0.17	–0.21	1.4 × 10 ^{–4}	49.22	51.35	54.98	59.75	60.02
Ni–Cr–P 15C	4.55	–0.26	–0.25	2.56 × 10 ^{–3}	–0.21	–0.20	5.3 × 10 ^{–4}	48.23	49.95	52.55	50.68	50.25
Ni–Cr–P 10C	1.75	–0.26	–0.24	8.4 × 10 ^{–3}	–0.26	–0.24	2.0 × 10 ^{–3}	45.48	49.81	48.23	46.55	45.05

sample shows in the order of 10^{–8} A/cm². Similarly, Tsai et al. [8] and Chiang et al. [9] demonstrated the performance of Ni-electroplated pack chromized AISI 1045 low-carbon steel as BPPs. The corrosion current of Ni-electroplated AISI 1045 sample shows the corrosion current in the range of 10^{–6} A/cm² and that of the pack chromized sample is 8.37 × 10^{–8} A/cm². Meanwhile, Jin et al. [10] showed that the corrosion current of both bare and Ni–P electroless coated mild steel samples is in the range of 10^{–6} A/cm². The difference in corrosion resistance is due to the difference in the simulated PEM fuel cell environment used for testing the corrosion resistance. The corrosion test was carried out in 0.5 M H₂SO₄ at room temperature [7–9, 12] or 0.5 M H₂SO₄ with 0.07 M Na₂SO₄ and 2 ppm HF at 50 °C [10]. These test conditions do not simulate the actual PEM fuel cell environment. PEM fuel cell operates at 80 °C and the SO₄^{2–} and F[–] ions from the electrolyte create an aggressive environment near the BPPs surface. Therefore, to understand the actual corrosion resistance, we evaluated the bipolar plate in an aqueous electrolyte of 0.5 M H₂SO₄ and 2.0 ppm HF at 80 °C. Hence, the data reported here by us may give a better assessment of the performance of bare and Ni–Cr–P coated AISI 1020 steel.

Interfacial contact resistance

Figure 8 shows the variation of ICR values of bare AISI 1020 and different Ni–Cr–P coatings electrodeposited at different temperatures varying the immersion time in a simulated PEM fuel cell environment. In the case of AISI 1020 low-carbon steel, ICR value decreased with time for the first 1 h of immersion period. The decrease in ICR value is due to the absence of passive layer forming metal in AISI 1020. The polarization studies corroborate the lack of passive layer in AISI 1020. With further increase in immersion period, the low-carbon steel completely dissolves in the simulated PEM fuel cell environment solution.

Initially, all Ni–Cr–P coated samples show an increase in ICR value with time, but the ICR value of Ni–Cr–P 15C and Ni–Cr–P 10C samples decreases after 2 h and 1 h of

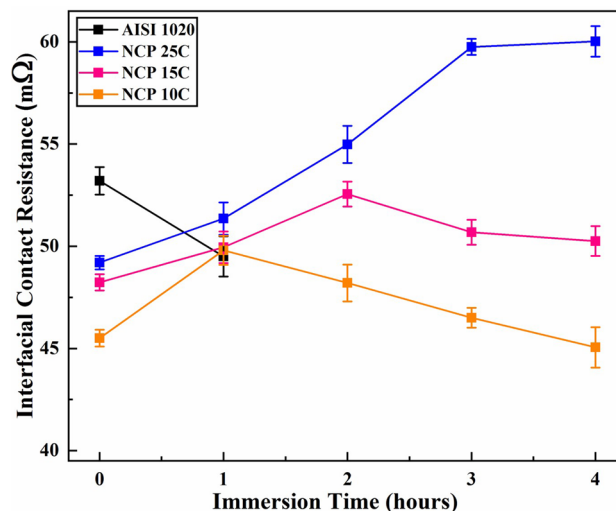


Fig. 8 Variation of interfacial contact resistance (ICR) of Ni–Cr–P coating samples and AISI 1020 bare substrate with an immersion time of samples in 0.5 M H₂SO₄ and 2 ppm HF at 80 °C

immersion time, respectively. The initial increment in the ICR value is mainly due to the presence of Cr in the samples, which forms a barrier layer consisting of Cr₂O₃. However, with an increase in immersion time, Cr₂O₃ in the barrier layer possibly converts to an inhomogeneous Cr(OH)₃ or hydrated oxide layer. These hydroxides or hydrated oxide layers dissolve in the solution and result in the formation of pits on the coating surface. In the case of Ni–Cr–P 25C coating, the ICR value increases gradually with immersion time. Similarly for Ni–Cr–P 25C coating, the ICR increases for the first 3 h of immersion and decreases thereafter. The increase in ICR is most likely due to the increase in the thickness of the passive layer. However, after 3 h of immersion period, the oxides in the passive layer most likely convert to hydrated oxides and dissolve into the solution. However, due to the higher amount of Cr in Ni–Cr–P 25C coatings, passive layer thickness does not decrease to that extent where it may affect the ICR value largely.

Conclusion

Cyclic voltammetry shows that it is difficult to reduce Cr^{+3} while Ni^{+2} directly reduces easily without any formation of intermediate complexes. The deposition rate of Cr was increased by adding ligands to the electrolyte. Ni–Cr–P coatings electrodeposited at pH 3.0 and room temperature (25 °C) were crack-free and adherent. Polarization studies show that the corrosion resistance of Ni–Cr–P coatings increases by several orders of magnitude with an increase in Cr content. The ICR of all Ni–Cr–P coatings increased with immersion time most likely due to the formation of hydrated oxide layers and subsequent formation of the pits on the surface of coated samples. The ICR of BPPs with Ni–Cr–P coatings is in the range, but the corrosion resistance is still one order lower than the US-DOE 2020 targets for PEM fuel cell bipolar plate. Although Ni–Cr–P coatings exhibit lower corrosion resistance and fractionally higher ICR value compared to US-DOE 2020 targets, this study shows that it is possible to reduce the overall manufacturing cost of BPPs using low-cost electroplating as a surface modification technique, and there is a scope to improve the corrosion resistance of BPPs by modifying the composition. The corrosion resistance of the BPPs can be further improved by incorporating transition metals such as molybdenum and cobalt into the coating as they form stable conducting oxides upon exposure to a PEM fuel cell working environment.

Acknowledgements UKC, SPP, and ADP are thankful to the Indian Institute of Technology (IIT) Bhubaneswar and Ministry of Human Resource Development (MHRD), Government of India (GOI) for providing financial support.

Open Access This article is distributed under the terms of the Creative Commons Attribution 4.0 International License (<http://creativecommons.org/licenses/by/4.0/>), which permits unrestricted use, distribution, and reproduction in any medium, provided you give appropriate credit to the original author(s) and the source, provide a link to the Creative Commons license, and indicate if changes were made.

References

1. Karimi, S., Fraser, N., Roberts, B., Foulkes, F.R.: A review of metallic bipolar plates for proton exchange membrane fuel cells: materials and fabrication methods. *Adv. Mater. Sci. Eng.* (2012). <https://doi.org/10.1155/2012/828070>
2. Technical Targets: Bipolar plates for transportation applications. <https://www.energy.gov/eere/fuelcells/doe-technical-targets-polymer-electrolyte-membrane-fuel-cell-components>. Accessed 10 May 2019
3. Lyons, K.S., Gould, B.D.: Lightweight titanium metal bipolar plates for PEM fuel cells. *Mater. Sci. Forum* **879**, 613–618 (2016). <https://doi.org/10.4028/www.scientific.net/MSF.879.613>
4. Parvanian, A.M., Panjepour, M.: Development of open pore copper foams to use as bipolar plates in polymer electrolyte

- membrane fuel cell stacks. *Iran. J. Energy Environ. (IJEE)* **4**, 99–103 (2013). <https://doi.org/10.5829/idosi.ijee.2013.04.02>
5. Palumbo, G., Piccininni, A.: Numerical-experimental investigations on the manufacturing of an aluminium bipolar plate for proton exchange membrane fuel cells by warm hydroforming. *Int. J. Adv. Manuf. Technol.* **69**, 731–742 (2013). <https://doi.org/10.1007/s00170-013-5047-1>
6. Papadias, D.D., Ahluwalia, R.K., Thomson, J.K., Meyer, H.M., Brady, M.P., Wang, H., Turner, J.A., Mukundan, R., Borup, R.: Degradation of SS316L bipolar plates in simulated fuel cell environment: corrosion rate, barrier film formation kinetics and contact resistance. *J. Power Sources* **273**, 1237–1249 (2015). <https://doi.org/10.1016/j.jpowsour.2014.02.053>
7. Bai, C.-Y., Lee, J.-L., Wen, T.-M., Hou, K.-H., Wu, M.-S., Ger, M.-D.: The characteristics of chromized 1020 steel with electrical discharge machining and Ni electroplating pretreatments. *Appl. Surf. Sci.* **257**, 3529–3537 (2011)
8. Tsai, L.C., Sheu, H.H., Chen, C.C., Ger, M.D.: The preparation of the chromized coatings on AISI 1045 carbon steel plate with the electroplating pretreatment of Ni or Ni/Cr–C film. *Int. J. Electrochem. Sci.* **10**, 317–331 (2015)
9. Chiang, T.Y., Ay-Su, Tsai, L.C., Lee, H.B., Lin, C.Y., Sheu, H.H., Chang, C.C.: Effect of metal bipolar plate channel fabrication on electroplating—using nickel electroplating of AISI 1045 channel substrate as an example. *Int. J. Electrochem. Sci.* **10**, 1926–1939 (2015)
10. Jin, J., Zheng, D., Liu, H.: The corrosion behavior and mechanical properties of CrN/NiP multilayer coated mild steel as bipolar plates for proton exchange membrane fuel cells. *Int. J. Hydrogen Energy* **42**, 28883–28897 (2017)
11. Jang, J., Choi, C., Kim, J., Park, Y.-D., Kang, N., Choi, Y.S., Nam, D.-G.: Surface characterization of chromium nitrided low carbon steel as bipolar plate for polymer electrolyte membrane fuel cell. *Sci. Adv. Mater.* **10**, 206–209 (2018)
12. Bai, C.Y., Ger, M.D., Wu, M.S.: Corrosion behaviors and contact resistances of the low-carbon steel bipolar plate with a chromized coating containing carbides and nitrides. *Int. J. Hydrogen Energy* **34**, 6778–6789 (2009). <https://doi.org/10.1016/j.ijhydene.2009.05.103>
13. Jin, C.K., Kang, C.G.: Fabrication by vacuum die casting and simulation of aluminum bipolar plates with micro-channels on both sides for proton exchange membrane (PEM) fuel cells. *Int. J. Hydrogen Energy* **37**, 1661–1676 (2012). <https://doi.org/10.1016/j.ijhydene.2011.10.050>
14. Nikam, V.V., Reddy, R.G.: Copper alloy bipolar plates for polymer electrolyte membrane fuel cell. *Electrochim. Acta* **51**, 6338–6345 (2006). <https://doi.org/10.1016/j.electacta.2006.04.019>
15. Cheng, X., Shi, Z., Glass, N., Zhang, L., Zhang, J., Song, D., Liu, Z.-S., Wang, H., Shen, J.: A review of PEM hydrogen fuel cell contamination: impacts, mechanisms, and mitigation. *J. Power Sources* **165**, 739–756 (2007)
16. González-Gutiérrez, A.G., Pech-Canul, M.A., Chan-Rosado, G., Sebastian, P.J.: Studies on the physical and electrochemical properties of Ni–P coating on commercial aluminum as bipolar plate in PEMFC. *Fuel* **235**, 1361–1367 (2019). <https://doi.org/10.1016/j.fuel.2018.08.104>
17. Peng, L., Yi, P., Lai, X.: Design and manufacturing of stainless steel bipolar plates for proton exchange membrane fuel cells. *Int. J. Hydrogen Energy* **39**, 21127–21153 (2014). <https://doi.org/10.1016/j.ijhydene.2014.08.113>
18. Yi, P., Peng, L., Feng, L., Gan, P., Lai, X.: Performance of a proton exchange membrane fuel cell stack using conductive amorphous carbon-coated 304 stainless steel bipolar plates. *J. Power Sources* **195**, 7061–7066 (2010). <https://doi.org/10.1016/j.jpowsour.2010.05.019>

19. Chanda, U.K., Behera, A., Roy, S., Pati, S.: Evaluation of Ni–Cr–P coatings electrodeposited on low carbon steel bipolar plates for polymer electrolyte membrane fuel cell. *Int. J. Hydrogen Energy* **43**, 23430–23440 (2018). <https://doi.org/10.1016/j.ijhydene.2018.10.218>
20. Clayton, C.R.: A bipolar model of the passivity of stainless steel: the role of mo addition. *J. Electrochem. Soc.* **133**, 2465 (1986). <https://doi.org/10.1149/1.2108451>
21. Lin, K.L., Hsu, C.J., Hsu, I.M., Chang, J.T.: Electroplating of Ni–Cr on steel with pulse plating. *J. Mater. Eng. Perform.* **1**, 359–361 (1992). <https://doi.org/10.1007/BF02652390>
22. Lin, K., Ho, J.: Electrodeposited Ni–Cr and Ni–Cr–P alloys. *ECS Trans.* **139**, 1305–1310 (1992)
23. Di Bari, G.A.: Electrodeposition of Nickel. *Modern Electroplating*, 5th edn, pp. 79–114. Wiley. (2011). <https://doi.org/10.1002/9780470602638.ch3>
24. Avasarala, B., Haldar, P.: Effect of surface roughness of composite bipolar plates on the contact resistance of a proton exchange membrane fuel cell. *J. Power Sources* **188**, 225–229 (2009). <https://doi.org/10.1016/j.jpowsour.2008.11.063>
25. Del Pianta, D., Frayret, J., Gleyzes, C., Cugnet, C., Dupin, J.C., Le Hecho, I.: Determination of the chromium(III) reduction mechanism during chromium electroplating. *Electrochim. Acta* **284**, 234–241 (2018). <https://doi.org/10.1016/j.electacta.2018.07.114>
26. Shashikala, A.R., Mayanna, S.M., Sharma, A.K.: Studies and characterisation of electroless Ni–Cr–P alloy coating. *Trans. IMF* **85**, 320–324 (2007)
27. Zeng, Z., Zhang, Y., Zhao, W., Zhang, J.: Role of complexing ligands in trivalent chromium electrodeposition. *Surf. Coat. Technol.* **205**, 4771–4775 (2011)
28. Protsenko, V., Danilov, F.: Kinetics and mechanism of chromium electrodeposition from formate and oxalate solutions of Cr(III) compounds. *Electrochim. Acta* **54**, 5666–5672 (2009)
29. Ren, X., Wei, Q., Zhe, L.I.U., Jun, L.I.U.: Electrodeposition conditions of metallic nickel in electrolytic membrane reactor. *Trans. Nonferrous Met. Soc. China* **22**, 467–475 (2012)
30. Aghdam, A.S., Allahkaram, S.R., Mahdavi, S.: Corrosion and tribological behavior of Ni–Cr alloy coatings electrodeposited on low carbon steel in Cr(III)–Ni(II) bath. *Surf. Coat. Technol.* **281**, 144–149 (2015)
31. Huang, C.A., Chen, C.Y., Hsu, C.C., Lin, C.S.: Characterization of Cr–Ni multilayers electroplated from a chromium(III)–nickel(II) bath using pulse current. *Scr. Mater.* **57**, 61–64 (2007). <https://doi.org/10.1016/j.scriptamat.2007.02.004>

Publisher's Note Springer Nature remains neutral with regard to jurisdictional claims in published maps and institutional affiliations.